Supplementary Information

Precision synthesis and atomistic analysis of deep blue cubic quantum dots made via self-organization

Authors: Olivier J. G. L. Chevalier[1], Takayuki Nakamuro[1]*, Wataru Sato[1], Satoru Miyashita[1], Takayuki Chiba[2], Junji Kido[2], Rui Shang[1]*, Eiichi Nakamura[1]*.

Affiliations:

[1] Department of Chemistry, The University of Tokyo, 7-3-1 Bunkyo-ku, Tokyo, 113-0033, Japan.

[2] Graduate School of Organic Materials Science, Yamagata University, Yonezawa, Yamagata, 992-8510, Japan.

*Corresponding authors. Email: muro@chem.s.u-tokyo.ac.jp, rui@chem.s.u-tokyo.ac.jp, nakamura@chem.s.u-tokyo.ac.jp.

Table of contents

Supplementary Notes

Supplementary Note 1: **Cs-QD$_4$**: neutral $Cs_{112}Pb_{64}Br_{240}$ vs. geometrically perfect $[Cs_{125}Pb_{64}Br_{240}]^{13+}$.

Cs-QD$_4$, $Cs_{112}Pb_{64}Br_{240}$, discussed in Fig. 1c, 5a, and 5b is an archetypal "neutral" lead perovskite QD$_4$, where all Pb atoms bear eight Br atoms and hence coordinatively saturated, and 112 negative charges are neutralized by 112 Cs cations[48,49]. Of these 112 Cs, 27 are located in the core of the QD, and 85 on the surface. A cautionary note is that this structure leaves some potential Cs cation sites vacant as illustrated in its side view in Fig. 5b, where we find only 10 Cs cations on the edge instead of 12. The formation of a structure of reduced symmetry arises from mismatch between the charge neutrality of **Cs-QD$_4$** and the geometry of the cube; that is, **Cs-QD$_4$** requires only 112 Cs cation, but the cubic geometry creates 125 potential Cs sites on the surface. On other word, if we fill all 125 sites by Cs cations, **Cs-QD$_4$** become $[Cs_{125}Pb_{64}Br_{240}]^{13+}$, which we do not necessarily consider here for species stably forming in a non-polar solvent such as toluene. Note that we find none of this problem in a bulk crystal where the number of Cs cation on edges is negligibly small.

Supplementary Note 2: Estimation of the size distribution of QDs on amorphous carbon (aC) film

The size distribution of the QDs on aC summarized in Fig. 4 was determined by using the standard deviation of the size determined by repeated measurement of single QDs of different sizes on aC (cf. Fig. 3b, Supplementary Fig. 10). This estimation should be valid because the QD are cubic as supported by the SMART-EM images (Fig. 5), and the QDs are defect-free and their surface fully coordinated by Br atoms as supported by the PLQY, EDX and SMART-EM data (Fig. 5). Note that the contrast of the MA, OAM, and OLA groups is too low to be detectable under the present TEM conditions, and hence Pb, Br, and Cs atoms can be seen (cf. Fig. 3a). As such, a QD$_3$ has 3 Pb atoms and 4 Br atoms edge wise, measuring 1.8 nm. Similarly, a QD$_4$ measures 2.4 nm, a QD$_5$ 3.0 nm and a QD$_6$ 3.6 nm. By measuring a single QD on aC, we can estimate a standard deviation on the QD measurement of 0.17 nm. We then use Gaussian distributions centered on each size. Line widths were adjusted to 0.17 nm and intensities were adjusted until the sum of gaussian functions best matched the total size distribution. Population fractions were estimated as a percentage of the area below the curve compared to the total area of the reconstructed size distribution.

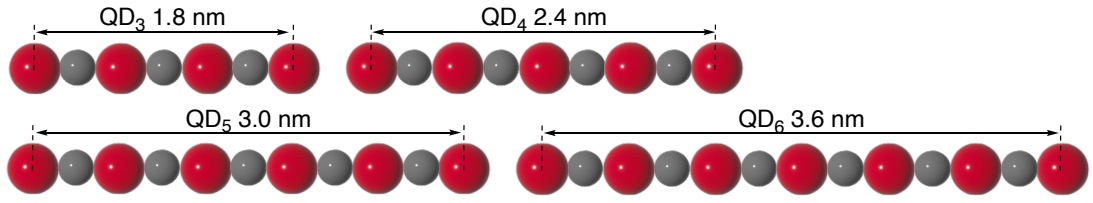

Supplementary Note 3: Estimation of the purity via photoluminescence spectra

First, we estimated the emitted wavelength for each one of the four species we identified in the size distribution analysis via the Brus equation. Namely, we fitted the following equation:

$$E(r) = E_{bulk} + \frac{h^2}{8r^2} * \frac{1}{\mu}$$

where h is Planck's constant, E_{bulk} = 2292 meV and μ = 0.127 m_e[50]. We factor in a deviation to ideality for the theoretical QD_3 estimated from the deviation seen with the experimental QD_4. We then used theoretical values for both QD_5 and QD_6 and Gaussian distributions centered on each wavelength. Linewidths and intensities were adjusted until the sum of gaussian functions best matched the photoluminescence spectra. Population fractions were estimated as a percentage of the area below the curve compared to the total area of the reconstructed PL spectra.

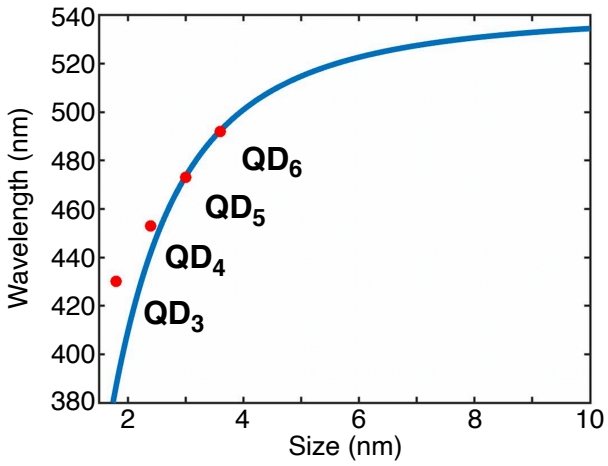

Supplementary Figures

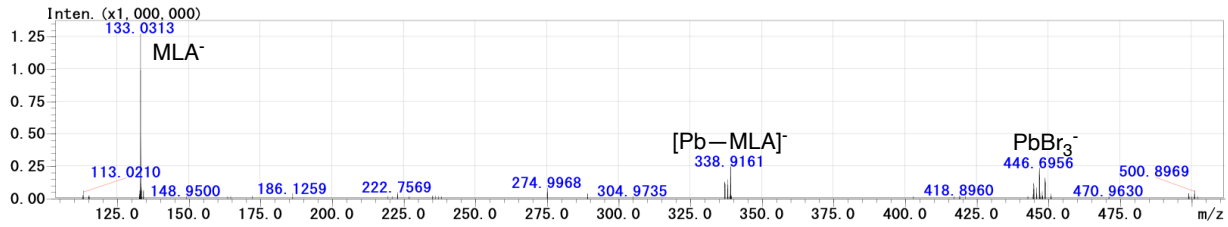

Supplementary Figure 1 | Negative ion mass spectra of the white precursor suspension, where we find three negative ions that serve as building blocks of the QD_4 as illustrated in Fig. 1d.

1:1 $PbBr_2$ MABr in DMF diluted with toluene without acid and amine

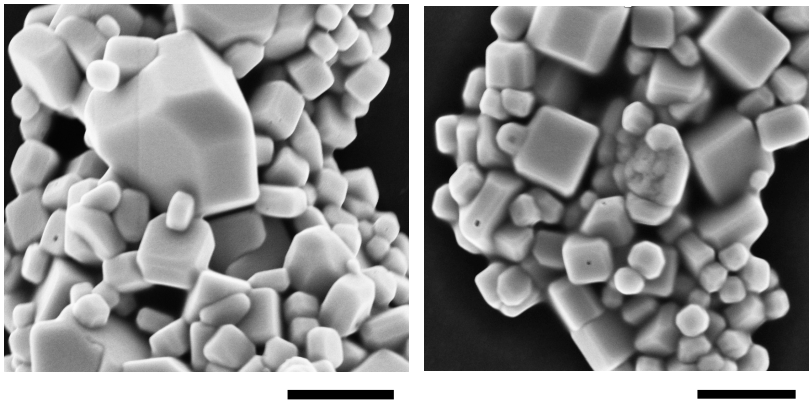

Supplementary Figure 2 | Representative SEM images of $MAPbBr_3$ microcrystals prepared without any ligands. Scale bars 500 nm.

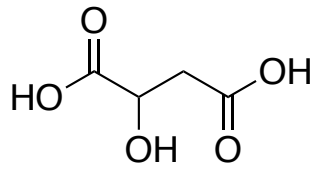

4.0 equiv malic acid
(MLA)

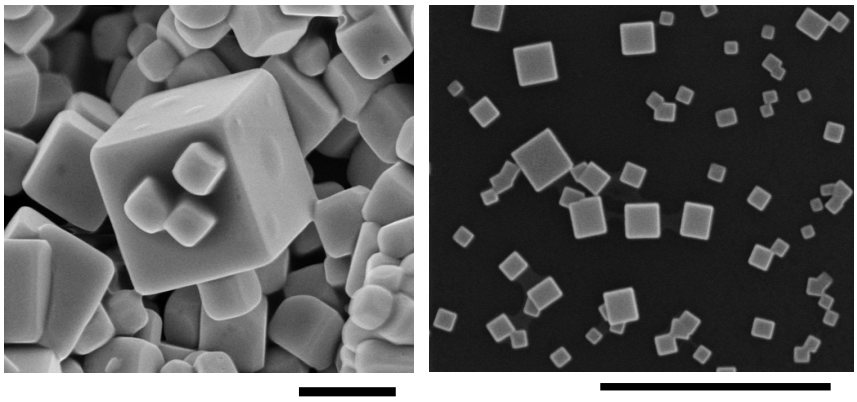

Supplementary Figure 3 | Representative SEM images of $MAPbBr_3$ microcrystals prepared with 4.0 equiv MLA to Pb. Scale bars 1 μm.

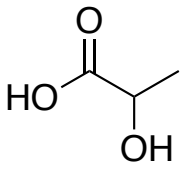

0.5 equiv lactic acid

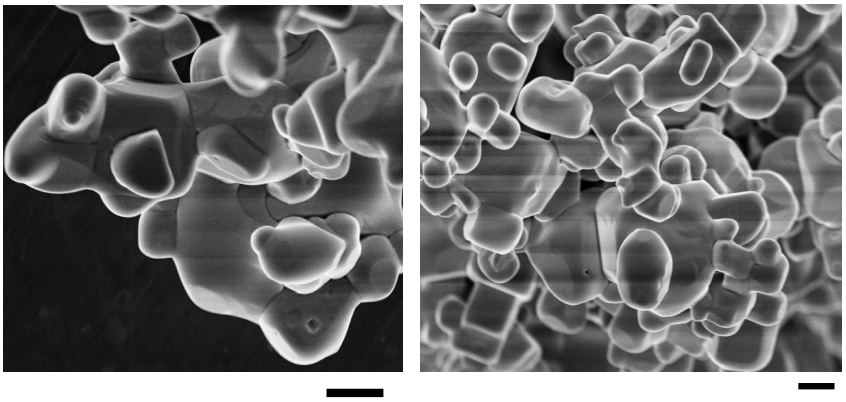

Supplementary Figure 4 | Representative SEM images of $MAPbBr_3$ microcrystals prepared with 0.5 equiv lactic acid to Pb. Scale bars 1 μm.

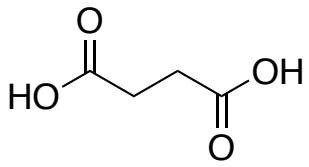

0.5 equiv succinic acid

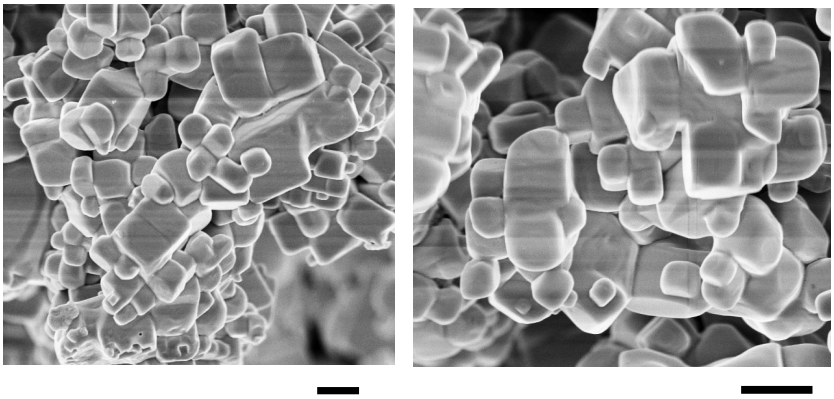

Supplementary Figure 5 | Representative SEM images of $MAPbBr_3$ microcrystals prepared with 0.5 equiv succinic acid to Pb. Scale bars 1 μm.

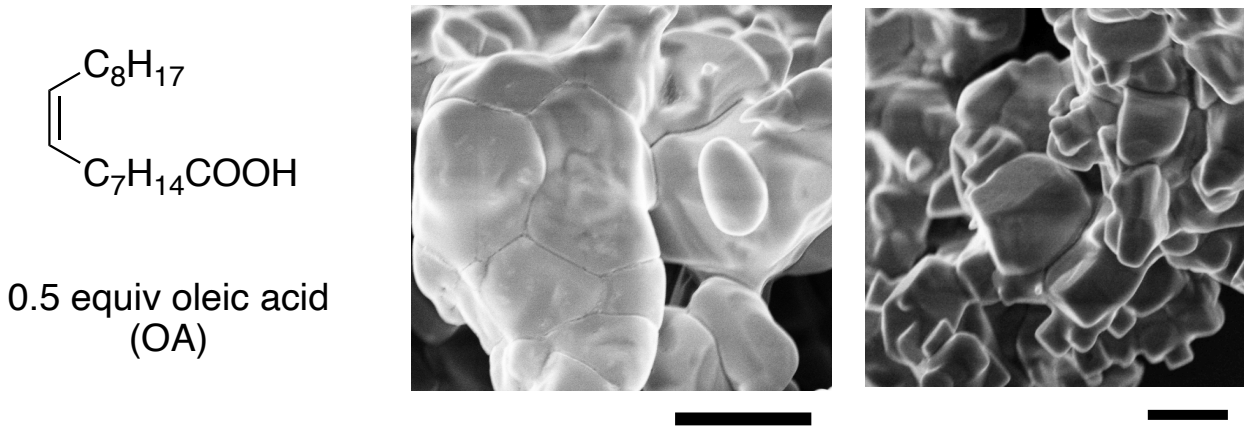

Supplementary Figure 6 | Representative SEM images of $MAPbBr_3$ microcrystals prepared with 0.5 equiv OA to Pb. Scale bars 1 μm.

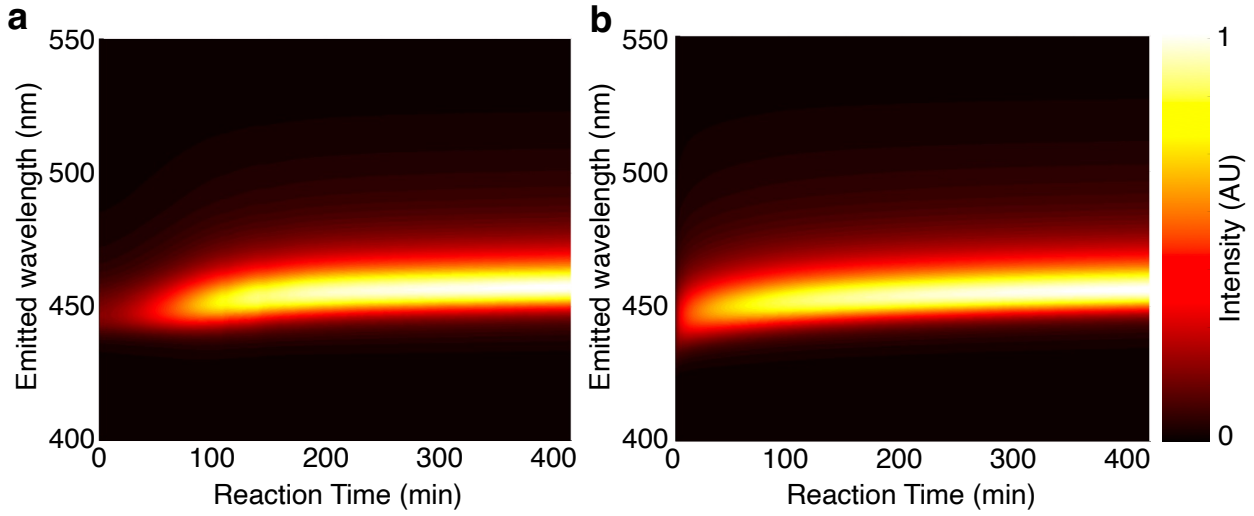

Supplementary Figure 7 | Heatmap of the reaction kinetics for the first 400 minutes. PL spectra were taken every 3 minutes over the course of the reaction for **a**, MLA•MA•QD_4 **(1)**, and **b**, OA•MA•QD_4 **(3)**.

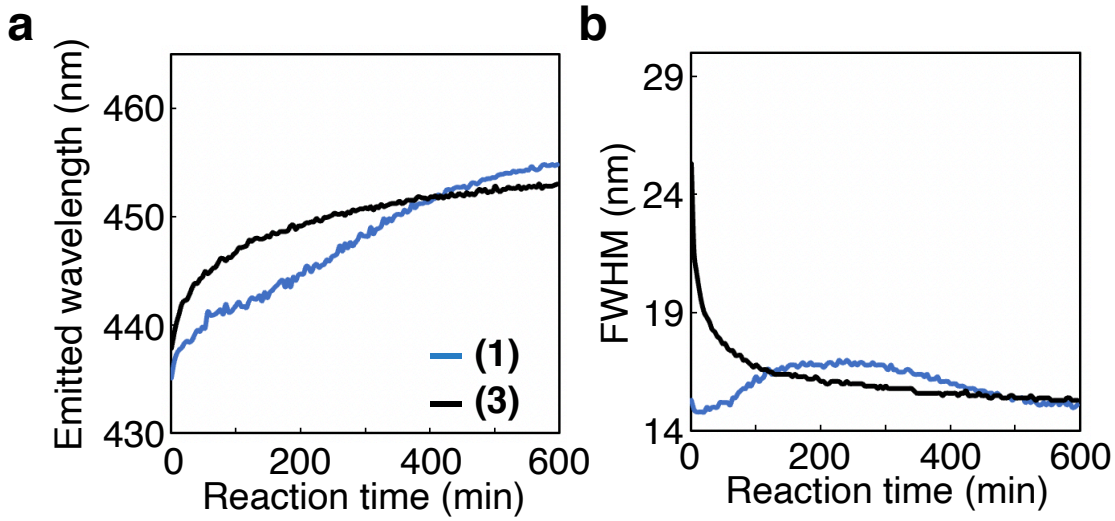

Supplementary Figure 8 | Evolution of the emitted wavelength **a**, and FWHM **b**, for **1** and **3** through the reaction, extracted from the heatmaps in the Supplementary Figure 7.

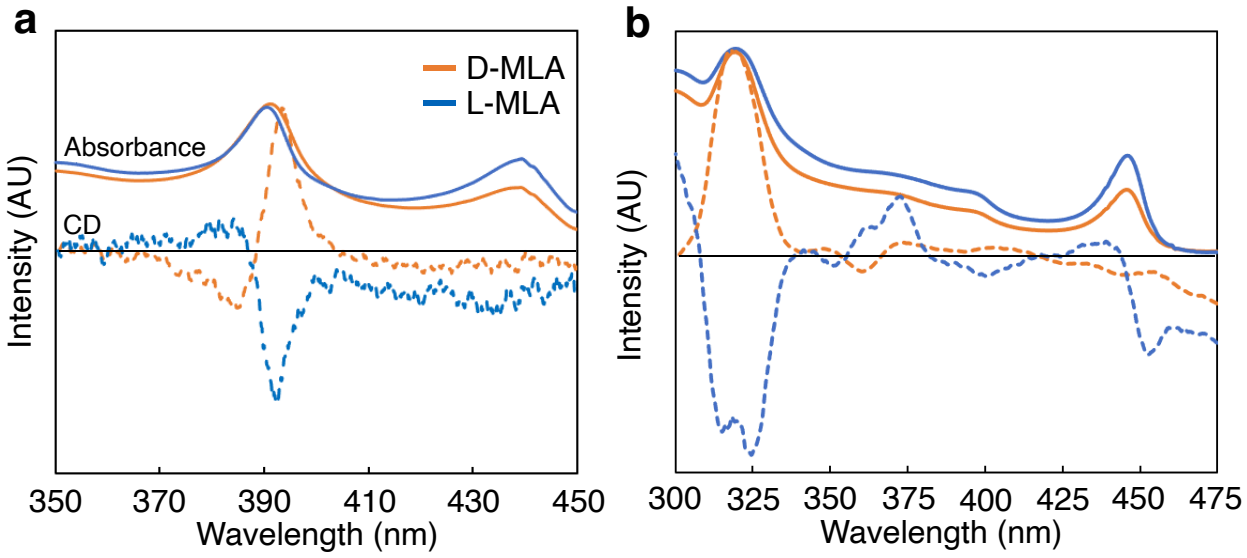

Supplementary Figure 9 | Circular dichroism and absorbance spectra with chiral MLA. **a**, MLA•MA•QD_4. **b**, MLA•Cs•QD_4.

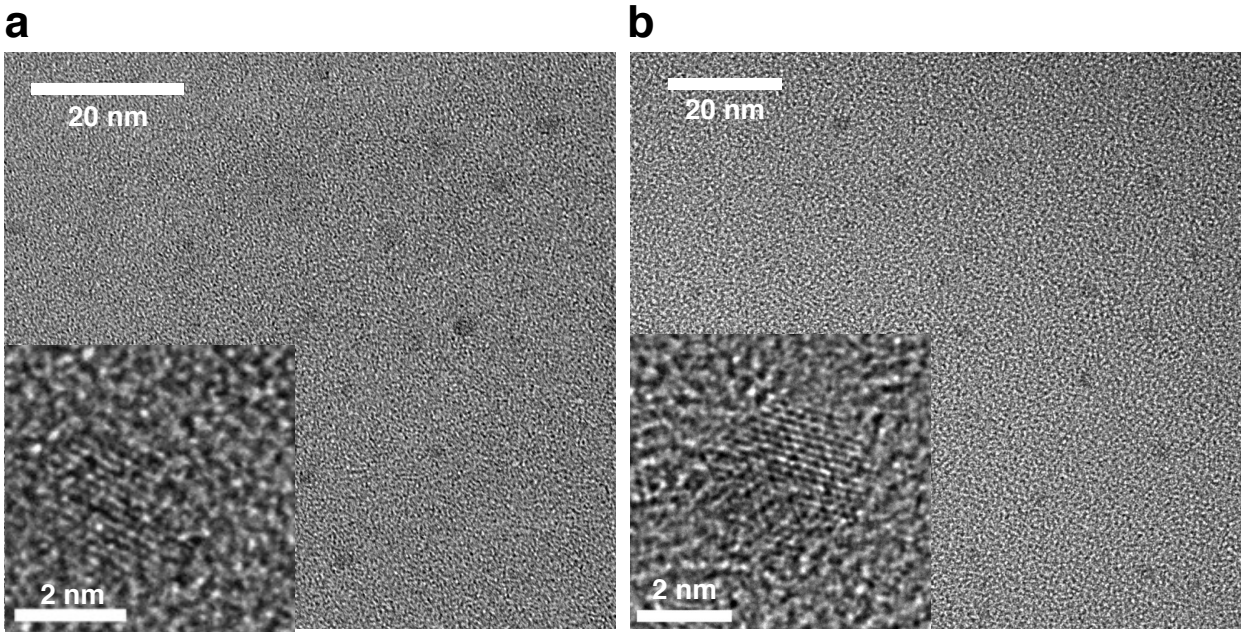

Supplementary Figure 10 | Representative TEM images of QDs on the surface of aC of 6 nm thickness. Low and high magnification of images are shown. **a**, MLA•MA•QD_4 (**1**). **b**, MLA•Cs•QD_4 (**2**).

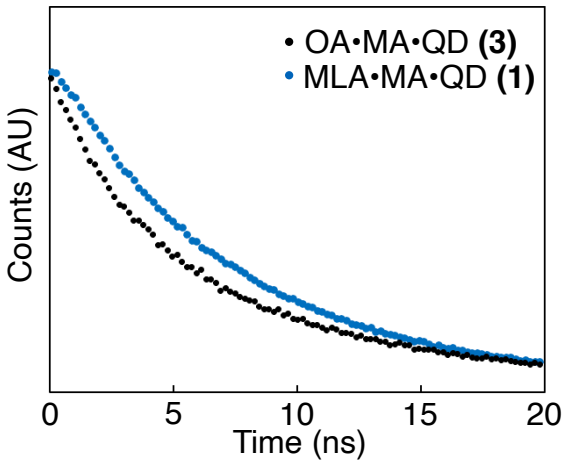

Ligand	A_1 (%)	τ_1 (ns)	A_2 (%)	τ_2 (ns)	$\langle\tau\rangle$ (ns)	k_r (x10^7 s^{-1})	k_{nr} (x10^7 s^{-1})	τ_r (ns)	τ_{nr} (ns)
OA•MA•QD	89.5	6.3	10.5	26.1	12.7	1.89	5.98	53	16.7
MLA•MA•QD	87.5	7	12.5	17.3	9.0	10.6	0.5	9.4	200

Supplementary Figure 11 | Fluorescence lifetime and results for a biexponential modeling.

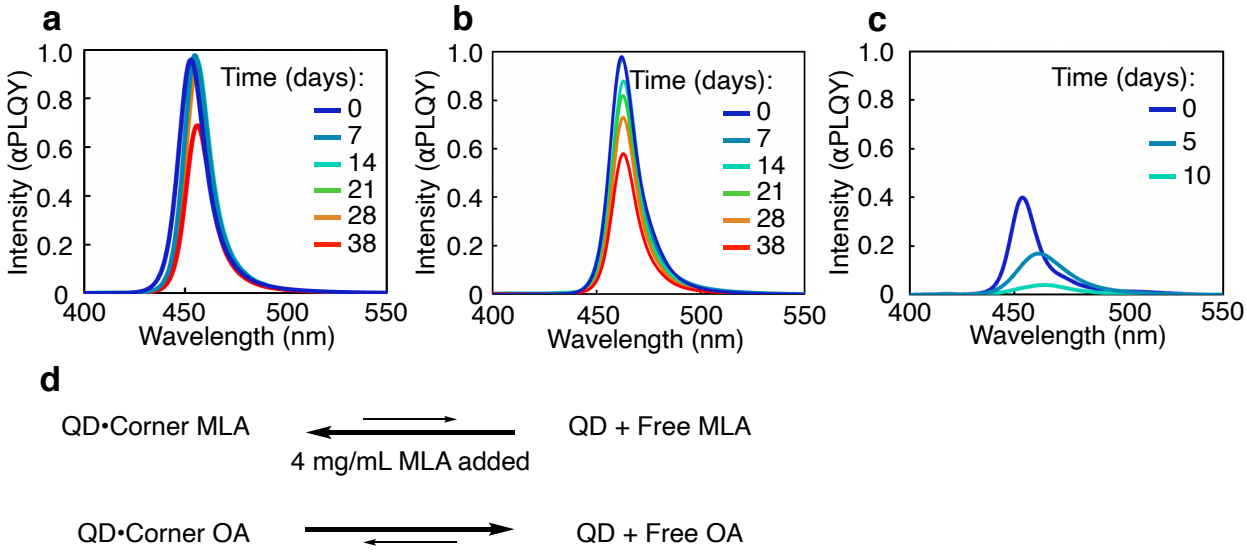

Supplementary Figure 12 | Fluorescence spectra through storage time at 5 °C for **a**, MLA•MA•QD_4 **(1)** in the presence of added MLA. **b**, MLA•Cs•QD_4 **(2)** in the presence of added MLA. **c**, OA•MA•QD_4 **(3)**. Intensity for each spectrum was set equal to the photoluminescence quantum yield. **d**, Addition of MLA displaces the equilibrium towards bound MLA, protecting the QD.

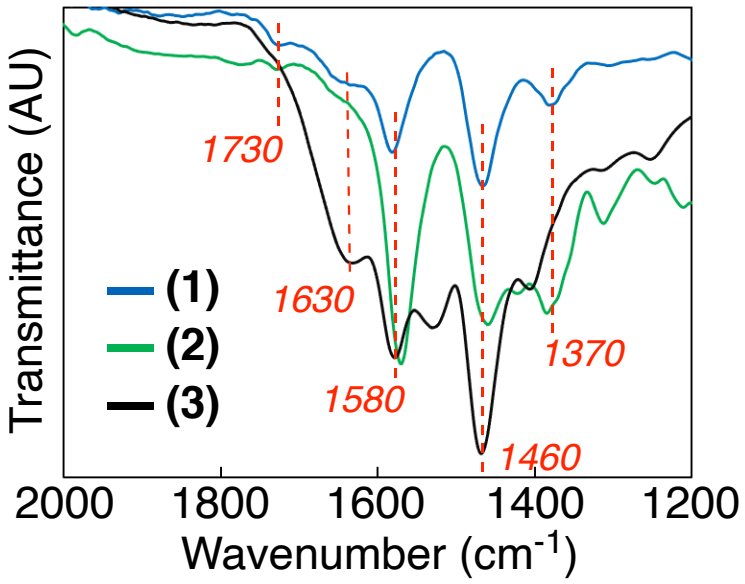

Supplementary Figure 13 | Film FTIR spectra for MLA•MA•QD_4 **(1)**, MLA•Cs•QD_4 **(2)** and OA•MA•QD_4 **(3)** Peaks are attributed as follow: C=O stretching (1730 cm^{-1}), N-H bending (1630 cm^{-1}), antisymmetric COO- stretching (1580 cm^{-1}), symmetric COO- stretching (1460 cm^{-1}) and alcohol O-H bending (1370 cm^{-1})[51].

Compound	O (eq to Pb)	Br (eq to Pb)	Cs (eq to Pb)	Ligand (eq to Pb)
MLA•MA•QD_4 **(1)**	0.7 ± 0.1	3.3 ± 0.1	-	0.14 ± 0.02
MLA•Cs•QD_4 **(2)**	0.75 ± 0.2	3.7 ± 0.1	0.9 ± 0.03	0.15 ± 0.03
OA•MA•QD_4 **(3)**	0.27 ± 0.02	3.0 ± 0.1	-	0.14 ± 0.01

Supplementary Figure 14 | EDX results using the amount of Pb as an internal standard. Results averaged over 20 measurements.

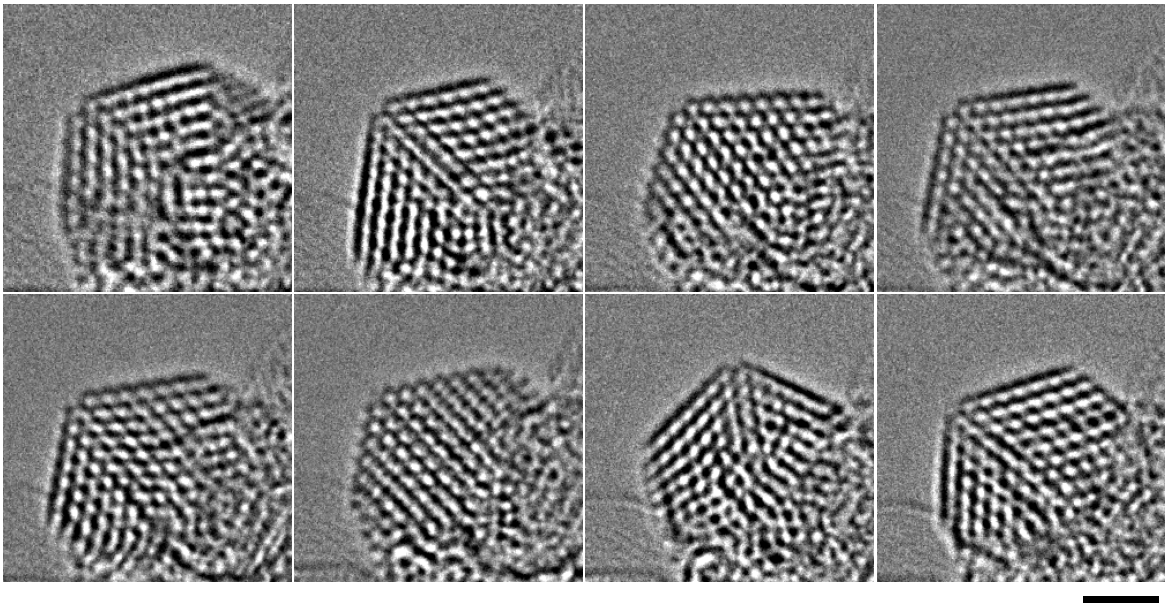

Supplementary Figure 15 | Representative SMART-EM images of **2** tumbling on CNT (Movie S1). EDR = 2.8×10^7 e^- nm^{-2} s^{-1}. Frame rate of 20.0 ms $frame^{-1}$ or 50 fps, and scale bar 1 nm.

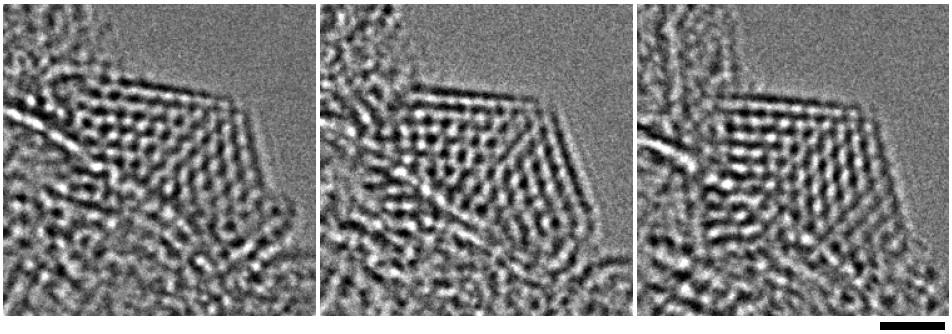

Supplementary Figure 16 | Representative SMART-EM images of **2** tumbling on CNT. EDR = 2.4×10^7 e^- nm^{-2} s^{-1}. Frame rate of 20.0 ms $frame^{-1}$ or 50 fps, and scale bar 1 nm.

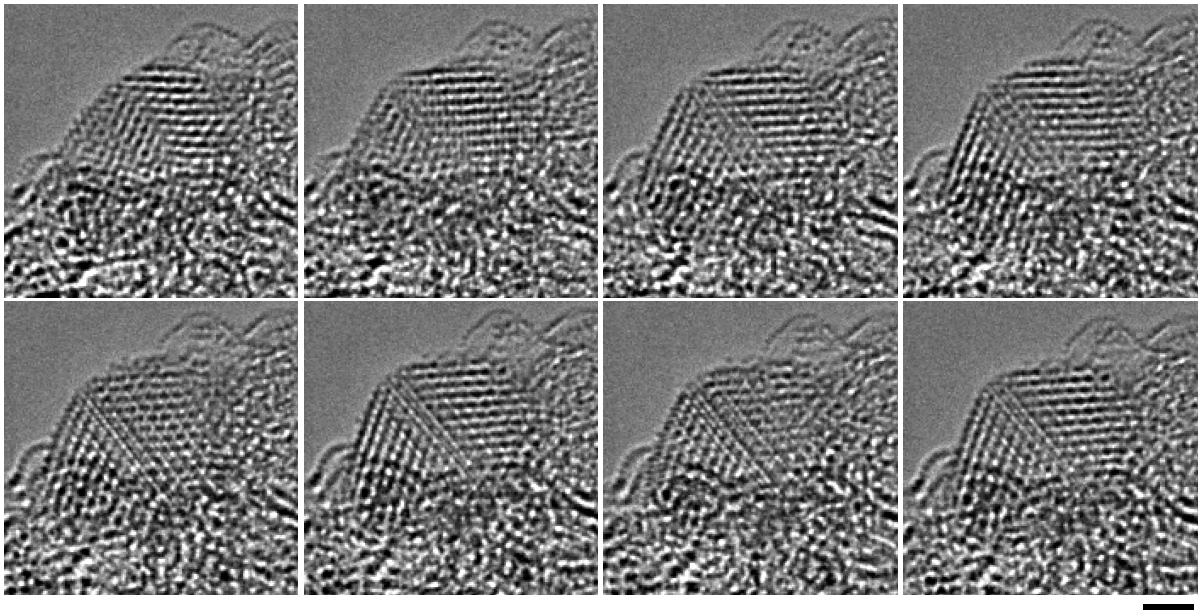

Supplementary Figure 17 | Representative SMART-EM images of **1** vibrating on CNT (Movie S3). EDR = 2.1×10^7 e^- nm^{-2} s^{-1}. Frame rate of 13.3 ms $frame^{-1}$ or 75 fps, and scale bar 1 nm.

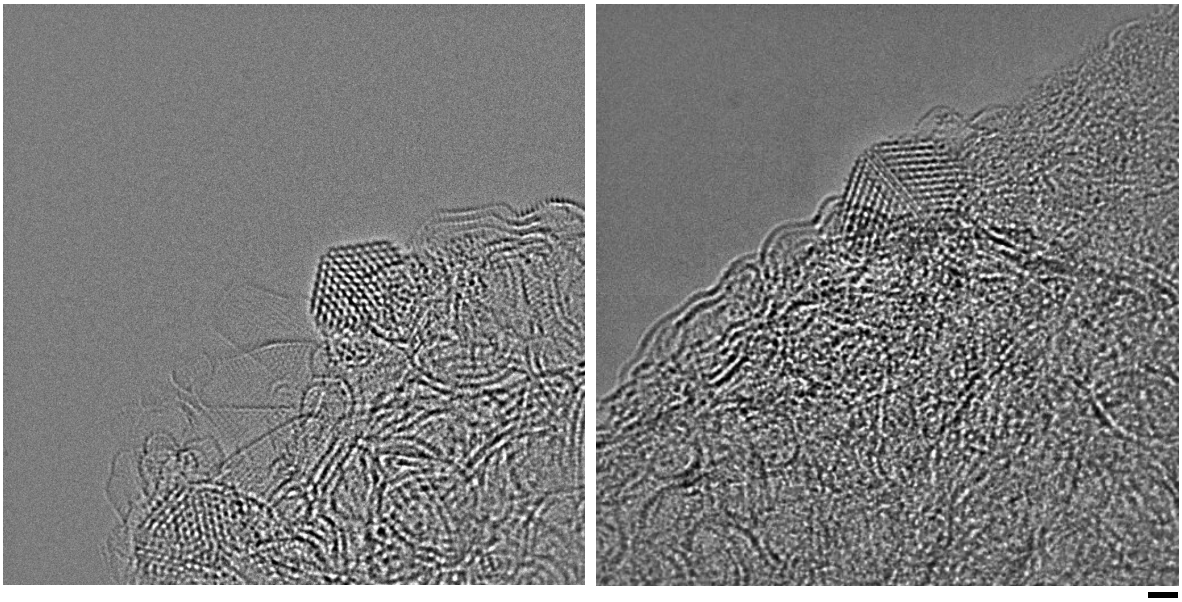

Supplementary Figure 18 | Overall views of QDs seen as a cube on the surface of aggregate of CNTs and graphitic structures observed by SMART-EM. Graphitic materials are more conductive by thousand times and hence more electron-donative than amorphous carbon film. Left: **2**. Right: **1**. The TEM scale was internally calibrated using the graphitic sites of CNTs. Scale bar 1 nm.

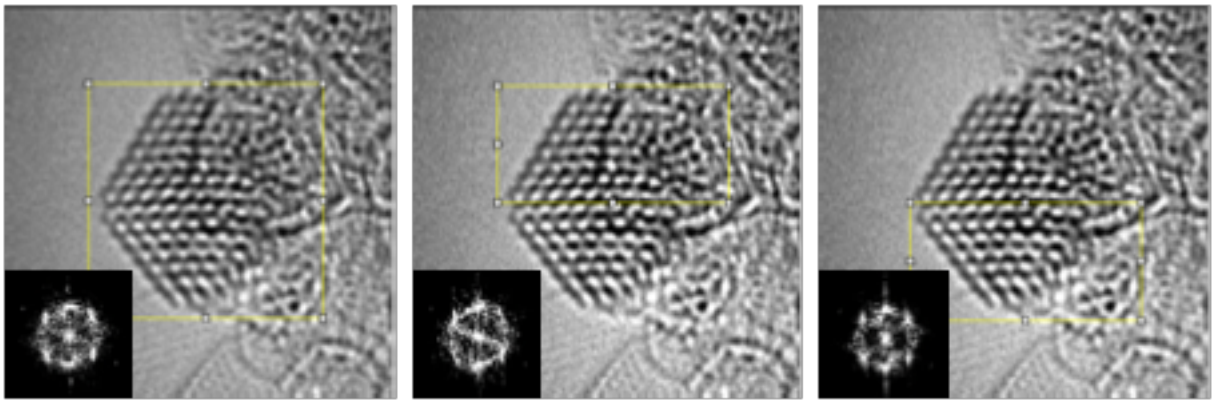

Supplementary Figure 19 | FFT patterns of **2**. We find the same pattern over different sections of the QD indicating that it is single crystal.

Captions for Video S1 to S3

Video S1. Structural fluctuation of **2** on CNT (**Fig. 5f-j**).

This is the movie of **2** on CNT without drift and rotation correction. The experimental conditions: Acceleration voltage of 80 kV, electron dose rate of 2.8×10^7 e^- nm^{-2} s^{-1}, and exposure time of 20.0 milliseconds for each frame. The playback speed of the video is 25 fps, half of the original video recording. Scale bar is 1 nm.

Video S2. Structural fluctuation of **1** on CNT (**Fig. 5l**).

This is the movie of **1** on CNT without drift and rotation correction. The experimental conditions: Acceleration voltage of 80 kV, electron dose rate of 2.6×10^7 e^- nm^{-2} s^{-1}, and exposure time of 5.0 milliseconds for each frame or 200 fps. The playback speed of the video is 50 fps. Scale bar is 1 nm.

Video S3. Structural fluctuation of **1** on CNT (**Fig. 5m-n**).

This is the movie of **1** on CNT without drift and rotation correction. The experimental conditions: Acceleration voltage of 80 kV, electron dose rate of 2.1×10^7 e^- nm^{-2} s^{-1}, and exposure time of 13.3 milliseconds for each frame. The playback speed of the video is 37.5 fps, half of the original video recording. Scale bar is 1 nm.

Supplementary References

[48] Ten Brinck, S. & Infante, I. Surface Termination, Morphology, and Bright Photoluminescence of Cesium Lead Halide Perovskite Nanocrystals. *ACS Energy Lett.* **1,** 1266-1272 (2016).

[49] Ravi, V. K. *et al.* Origin of the Substitution Mechanism for the Binding of Organic Ligands on the Surface of $CsPbBr_3$ Perovskite Nanocubes. *J. Phys. Chem. Lett.* **8**, 4988-4994 (2017).

[50] Galkowski, K. et al. Determination of the exciton binding energy and effective masses for methylammonium and formamidinium lead tri-halide perovskite semiconductors. *Energy Environ. Sci.* **9**, 962-970 (2016).

[51] Oomens, J. & Steill, J. D. Free Carboxylates Stretching Modes. *J. Phys. Chem. A* **112**, 3281-3283 (2008).